Friction

Research Article

Enhanced dispersion stability of shear thickening fluid based on PS@ZIF-8 core–shell nanospheres and ionic liquids for functional applications

Bingbing Lai[1,2], Jianglin Yin[3], Qin Zhao[1,✉], Mengke Zhang[1,2], Gaiqing Zhao[1,2,✉], Xiaobo Wang[1,2]

Cite this article: Lai BB, Yin JL, Zhao Q, et al. *Friction* 2026, **14**(1): 9441068. https://doi.org/10.26599/FRICT.2025.9441068

ABSTRACT: Material failure caused by load impacts frequently results in significant economic losses and negative effects. The application expansion of shear thickening fluid (STF) under special impact conditions is expected to lead to the design of a prospective impact-resistant structure because of its shear thickening effect, with an instantaneous response and reversible viscosity change. Herein, core–shell nanospheres (PS@ZIF-8) were synthesized using polystyrene (PS) nanoparticles as the base template. PS@ZIF-8 was used as the unique dispersed phase and was introduced uniformly into hydroxyl-functionalized ionic liquids (ILs) via simple ball mill dispersion to obtain novel STF systems. The performance of novel STF systems, such as the critical shear viscosity and peak viscosity, could be enhanced with increasing PS@ZIF-8 content. Importantly, the STF systems retained a significant shear thickening effect even after several shear scanning cycles because of the interaction between the dispersed phase (PS@ZIF-8) and the dispersion medium (ILs). The structural stability of PS@ZIF-8 in ionic liquids was also investigated, and the STF suspensions exhibited excellent stability in quantitative comparison experiments after centrifugal disruption at 8,000 r/min and standing for 60 days. In addition, a loading impact experimental method was developed to better investigate the anti-impact-wear performance of STF systems filled with limited space. The results of the tests revealed that the novel STF systems had outstanding flexibility in terms of energy absorption capacity and impact wear resistance. This study provides a strategy to prevent material failure under load impact and highlights the potential of these novel STF systems for designing efficient and stable impact-resistant structures.

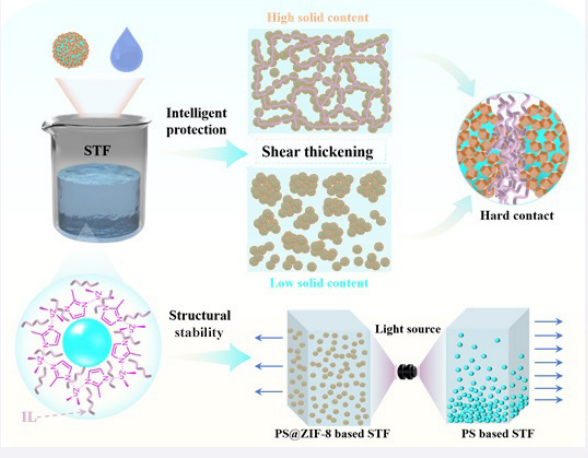

KEYWORDS: shear thickening fluid (STF); PS@ZIF-8; rheological properties; impact resistance; dispersion stability

1 Introduction

Impact and wear are widespread in all types of machinery in manufacturing and engineering, and materials are inevitably threatened by a variety of impact loads in service [1–4]. Impact loads are the most important factors for material wear. Among the types of wear failure, reciprocating impact on the material surface is a more common form of wear failure and the most unfavorable type of contact damage to the material. Impact loading can cause damage to contact surfaces, which, in the worst case, can lead to the failure of machine components [5, 6]. Extensive studies have been conducted on the wear of lubricating materials under frictional conditions such as rolling and sliding [7, 8]. However, as the most unfavorable type of wear failure, research on impact resistance and wear protection has not been widely conducted, especially the development of new protective materials under impact conditions.

Shear thickening fluid (STF), as the name suggests, is a kind of non-Newtonian fluid intelligent material that typically exists in dense suspension systems composed of dispersed solid particles in a liquid carrier [9, 10]. When the STF is subjected to shear beyond the critical shear rate, the system viscosity of the STF can rapidly increase by orders of magnitude, even when it transitions from a viscous fluid to a solid-like fluid. When the external stress is removed, the system returns to its initial state [11]. This transformation process is resistant to impact and results in energy dissipation [12]. The STF has excellent self-adaptability and

[1] State Key Laboratory of Solid Lubrication, Lanzhou Institute of Chemical Physics, Chinese Academy of Sciences, Lanzhou 730000, China. [2] Qingdao Center of Resource Chemistry and New Materials, Qingdao 266100, China. [3] Qingdao Lubemater Lubrication Material Technology Co., Ltd., Qingdao 266100, China.

✉ Corresponding authors. E-mail: Q. Zhao, zhaoqin@licp.cas.cn; G. Zhao, gqzhao@licp.cas.cn

Received: October 13, 2024; Revised: January 1, 2025; Accepted: January 22, 2025

reversibility. Therefore, introducing intelligent responsive materials under impact conditions to improve impact properties and wear protection offers significant application prospects.

The commonly used dispersed phase particles in STFs are silica (SiO_2) [13–16], calcium carbonate ($CaCO_3$) [17, 18], titanium dioxide (TiO_2) [19, 20], and other inorganic particles. Carrier liquids are usually polar or weakly polar solutions, such as water, small-molecule polyols, and polyethylene glycol (PEG) [21, 22]. SiO_2/PEG composite dispersion systems are the most common shear thickening systems. However, two major factors greatly limit the application of STF in harsh environments. One is the volatility and flammability of traditional liquid carriers, and the other is the weak shear thickening performance caused by the settling and separation of dispersed phase particles [23]. Recently, synthetic polymer particles, such as poly(methyl methacrylate) (PMMA) [24], polystyrene (PS) [25, 26], and polystyrene ethyl acrylate (PSt-EA) [27], have been used as dispersed phases to prepare new shear thickening systems. Nevertheless, these dispersed phase particles are prone to autoagglomeration, which significantly affects the dispersion stability and shear thickening performance of the STF. In addition, the STF is also limited by the weak interfacial interactions between the dispersed phase and the dispersion medium, density differences, and polarity mismatch behavior, which hinder the innovative application of the STF.

The zeolite imidazolate ester framework material ZIF-8 is one of the most common and widely studied metal organic framework (MOF) materials and is obtained by coordinating Zn^{2+} ions with dimethylimidazole. Owing to its unique cavity structure, ZIF-8 can be effectively utilized to encapsulate, isolate, and restrict many materials from small molecules to biomolecules, which are mostly used as carrier materials in fields such as separation, catalysis, and sterilization [28–30]. Recent attempts in the field of lubrication, which can effectively expand its application areas [31–34], have increased. To achieve high-performance STF systems in impact wear fields, our first study showed that introducing nonspherical imidazolium zeolitic frame-8 (ZIF-8) nanoparticles as additive phases was an effective strategy that can overcome the traditional inability of STFs to achieve effective shear thickening effects from a single design [35]. However, in this multiphase shear thickening strategy involving simple mixing of ZIF-8, it is still difficult to achieve good dispersibility of dispersed phase materials in liquid carriers (Fig. 1(a)). Therefore, there is an urgent need to prepare new STF systems to coordinate the shear thickening effect and dispersion stability. Surface modification of dispersed phase particles with ZIF-8 to obtain nanocomposites with special properties may be a more effective strategy (Fig. 1(b)). ZIF-8 can reduce the surface energy of the dispersed phase, increase the steric hindrance effect, prevent agglomeration and precipitation in the suspension, and improve the performance of the STF by utilizing its own performance advantages. Furthermore, from the perspective of dispersion media, highly polar ionic liquids (ILs) exhibit superior performance in the preparation of STF samples as dispersion media because of their advantages of good thermal stability, special solubility, nonflammability, and well-designed molecular structure [36–39], laying the foundation for high performance and stability in the use of dense particulate suspensions.

In this work, to overcome the obstacles of traditional STFs, such as volatilization of dispersing media and sedimentation of dispersed phase particles, they were applied in the field of impact wear protection. A core–shell nanosphere, PS@ZIF-8, was synthesized as a dispersed phase on the basis of the PS microspheres, and a green solvent with excellent properties, a hydroxyl-functionalized ionic liquid (1-hydroxylethyl-3-methylimidazolium bis(trifluoromethanesulfonyl)imide), was used as the dispersing medium. Thus, a new high-performance PS@ZIF-8-IL-based STF was successfully constructed via a simple and convenient ball-milling dispersion method (Fig. 1(c)). The effects of the dispersed phase concentration and the number of shear scanning cycles on the steady-state and dynamic rheological properties of the STF samples were investigated, and the mechanism of shear thickening was elucidated. Dispersion stability experiments revealed that the prepared composite structure-based suspension system had better gravitational and colloidal stability than did the pure PS-based dispersion system, indicating good prospects for use under harsh working conditions. In addition, the impact wear resistance of the STF samples was evaluated via a reciprocating impact test (Fig. 1(d)). The results show that an STF can utilize its shear-thickening effect to exhibit good impact and wear protection properties in filled structures under impact. While increasing versatility, the impact resistance behavior and protection mechanism of the STF are revealed.

2 Experimental

2.1 Materials

2-Methylimidazole (2-MIm; 98%, Aladdin, China), zinc acetate dihydrate ($CH_3COOZnOOCCH_3{\cdot}2H_2O$, 98%, Aladdin, China), 1-hydroxylethyl-3-methylimidazolium bis(trifluoromethanesulfonyl) imide([HOEtMI][NTf_2]; 97%, Aladdin, China), styrene (St; Sinopharm, China), polyvinyl pyrrolidone (PVP; Sinopharm, China), 2,2′ -azobis(2-methylpropionitrile) (AIBN; Sinopharm, China), anhydrous ethanol (EtOH; Sinopharm) and methanol (MeOH, Sinopharm, China) were purchased from commercial sources and used without further purification.

2.2 Synthesis of PS@ZIF-8

PS microspheres were prepared via previously reported methods [40], and the details are as follows. St (10.0 g), PVP (1.5 g), and AIBN (0.1 g) were subsequently weighed and dissolved in EtOH (100.0 g). The mixture was then deoxygenated by passing through nitrogen for 30 min at room temperature to ensure that the reaction was conducted in an oxygen-free environment. The above mixture was stirred for 12 h at 70 °C at 600 r/min. The product was collected by means of centrifugation and purified by washing with ethanol three times. Finally, the PS was obtained and used for the next step after drying for 12 h under vacuum at 80 °C.

The procedures used to fabricate PS@ZIF-8 are shown in Fig. 1(b). The obtained PS (0.5 g) was dispersed into a MeOH mixture (90 mL within 1 g of PVP). The above mixture was strongly stirred for 30 min and sonicated for 10 min, alternately for a total of 3 h. Then, zinc acetate dihydrate (6 g) and 2-MIm (7 g) were dissolved in MeOH (100 mL) to form solutions. The methanol solution (zinc acetate dihydrate) was first poured into the PS solution and stirred for 30 min. Then, the methanol solution (2-MeIm) was added, and the mixture was stirred for another 6 h at room temperature. The mixed solutions were subsequently centrifuged, and the lower solid layer was subsequently washed several times with MeOH. Finally, PS@ZIF-8 was obtained by drying at 60 °C.

2.3 Preparation of the STF samples

The hydroxyl-functionalized ionic liquid [HOEtMI][NTf_2] was used as the dispersing medium, and the PS@ZIF-8 particles were used as the dispersing phase. A certain number of PS@ZIF-8

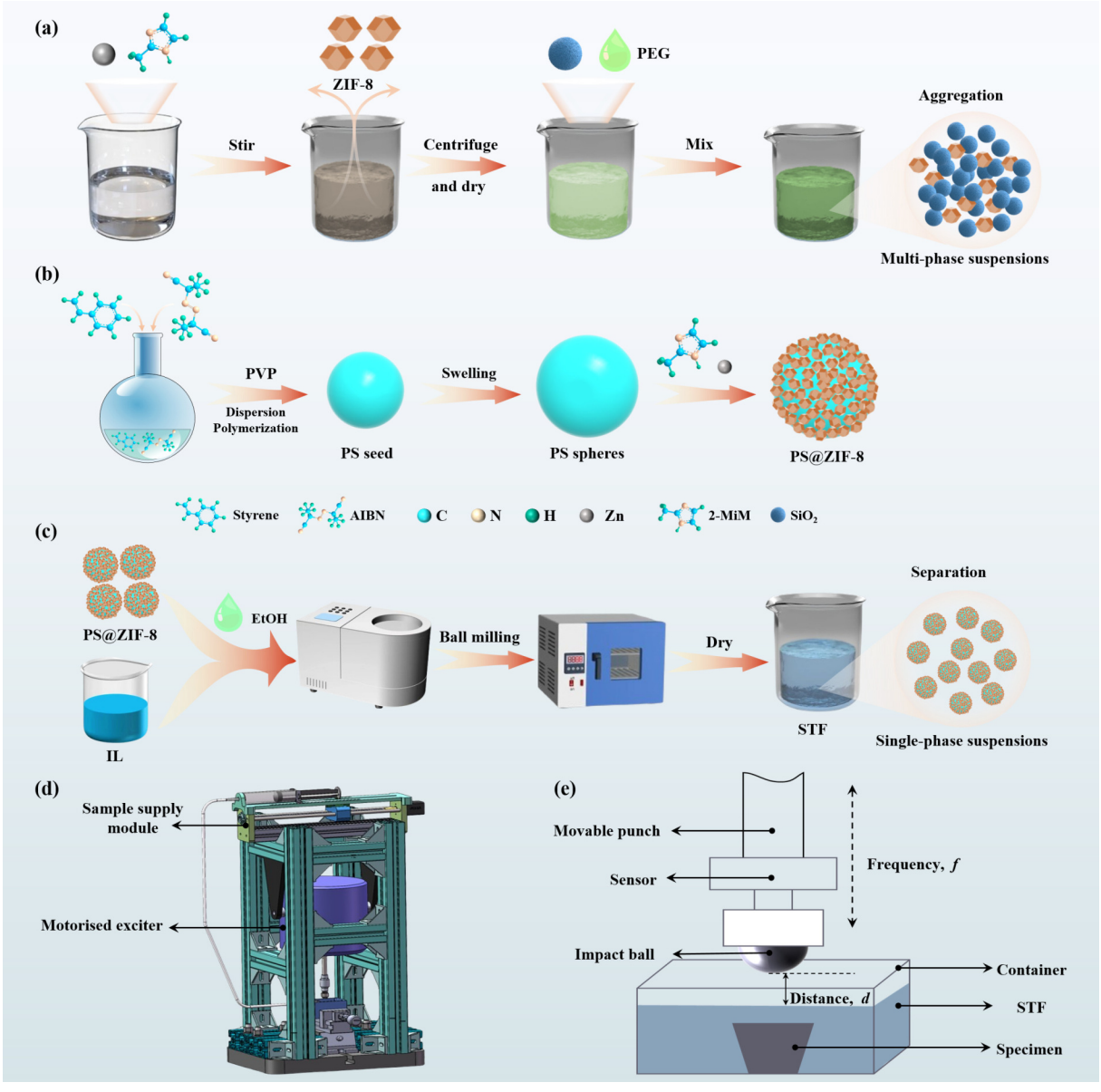

Fig. 1 Schematic diagram of preparations for (a) multiphase STF samples, (b) PS@ZIF-8, and (c) single-phase STF samples. (d) Controlable load impact wear testing machine. (e) Schematic diagram of the low-frequency impact test of the STF samples.

particles and [HOEtMI] [NTf_2] were added to a ball milling jar and diluted with a small amount of EtOH. The mixture was subsequently milled by using a lightweight planetary ball mill for 8 h at room temperature. Finally, the uniformly dispersed suspension was placed and dried in a vacuum drying oven (60 °C) for 12 h to remove the gas and EtOH, and then the STF was obtained (Fig. 1(c)). Five different ratios of STF were obtained by adjusting the ratio (56%, 60%, 64%, 68%, and 72%) of the dispersed phase particles to the ionic liquid. To ensure that the STF samples had good liquidity, the maximum proportion of PS@ZIF-8 in the ILs was adjusted to 72% (Table S1 in the Electronic Supplementary Material (ESM)).

2.4 Characterization of PS@ZIF-8

The crystal structure and crystallization behavior of the dispersed phase particles were characterized via an X-ray powder diffractometer (XRD; D8 Advance, Bruker, Germany). The thermal stability of the dispersed phase particles was also analyzed via a thermal analyzer (STA 449F3, NETZSCH, Germany). The infrared (IR) spectra of the dispersed phase particles were measured with a Fourier transform infrared spectrometer (FT-IR; TENSOR 27, Bruker, Germany). The microstructures of PS@ZIF-8 were examined by a scanning electron microscope (SEM; EVO 10, Zeiss, Germany).

2.5 Rheological test of the STF samples

The rheological properties of the STF samples were determined via a rotational rheometer (MCR302, Anton-Paar, Austria) with a cone-plate structure CP25-2/TG. The steady-state rheological tests and dynamic stress scans were performed three times at shear rates (0.01–1,000 s^{-1}) and in the strain range (0.1%–1,000%) at 10 Hz. The measurement temperature was maintained by an automatic temperature control device at 25 °C.

2.6 Dispersion stability test of the STF samples

The STF samples were diluted, and the dispersion stability of the samples after 24 h of standing was studied via a ultraviolet–visible (UV-Vis) spectrometer (TU-1810DSPC, Beijing General

Instrument Co., Ltd., China) with light wavelength (λ) = 680 nm. The sample (10 mL) was added to a sealed cylindrical glass vial and left at room temperature, and the top clear liquid volume V (mL) of the STF was periodically measured. The stability coefficient (k) was calculated via Eq. (1), and the larger k is, the better the stability of the nanofluid dispersion.

$$k = \frac{10 - V}{V} \quad (1)$$

The stability of a suspension can also be confirmed via the zeta values (Malvern Zetasizer Nano ZS90, UK), which are important parameters.

2.7 Impact experiments of the STF samples

The anti-impact-wear capacity of the STF samples was evaluated by a vertical load impact test rig. The impact test device is a shaker-driven device (Fig. 1(d)). The system consists of an arbitrary waveform generator that produces a continuous signal at a specified frequency, which is fed into an electric shaker through a power amplifier. The shaker consists of a spring, a moving coil, a core, etc. The moving coil produces an excitation force under the action of a variable-frequency current, which drives the excitation top bar and the punch mounted at the end of the top bar to perform up-and-down movement at the given frequency, and the punch contacts the test specimen and then reacts on the sensors to produce the corresponding electric charge. The charge is amplified and sent to the industrial control machine, and the experimental value is obtained through the acquisition program. The impact contact mode is ball-piece point contact, the upper test ball is a GCr15 steel ball (Fig. S1 in the ESM), the lower test piece is stainless steel, the diameter of the upper test ball is 10 mm, the distance from the punch to the upper surface of the STF is d (10 mm), the test time is 30 min, and the impact frequency is f (4 Hz) (Fig. 1(e)). After the load impact test, the wear volumes of the test pieces were measured via an interferometric noncontact surface profiler (MicroXAM-3D, KLA-Tencor, USA), and the impact and wear protection performances of the filled STF samples in a limited space were evaluated.

3 Results and discussion

3.1 Characterization and analysis of PS@ZIF-8

To confirm the morphological changes of ZIF-8 successfully encapsulated on PS, SEM image analysis of the prepared samples was performed to understand their morphology and structure. As shown in Fig. 2(a), the surface of the synthesized PS particles was very smooth, with micron-sized particles ranging from 1 to 2 μm (Fig. S2 in the ESM), and all the particles had a uniform spherical morphology and good dispersion. The SEM images in Figs. 2(b) and 2(c) show the *in situ* growth of composite nanoshells (ZIF-8) on the PS templates, and the PS particles were successfully encapsulated by the ZIF-8 polyhedral nanoparticles. The PS@ZIF-8 particles formed a unique micro/nanolayer structure with rough surfaces, which improved the interactions of the dispersed phases in the shear-thickened suspension system. Figure 2(d) shows the elemental mapping, with the elements C, N, and Zn uniformly distributed throughout the PS@ZIF-8 structure, which verifies the successful synthesis of the core–shell structure of PS@ZIF-8.

The XRD patterns of different nanoparticles are shown in Fig. 3(a), and the ZIF-8 sample exhibited sharp characteristic peaks, indicating that the synthesized ZIF-8 nanoparticles had good purity and crystallinity [29]. Compared with those of the ZIF-8 sample, the PS@ZIF-8 samples presented the same characteristic diffraction peaks, indicating that the introduction of PS did not change the crystal structure of the ZIF-8 nanoparticles. Figure 3(b) shows the infrared absorption peak of the PS@ZIF-8 particles. The peak at 420 cm^{-1} for ZIF-8 and PS@ZIF-8 represented the Zn–N bond stretching vibration. The peak at 2,930 cm^{-1} was attributed to the C–H bond stretching vibration generated on the imidazole ring, and the peaks at 1,308 and 1,146 cm^{-1} were related to the bending vibration of the imidazole ring. The peaks at 1,601, 1,492, and 1,452 cm^{-1} for PS and PS@ZIF-8 were attributed to stretching vibrations of the benzene ring backbone [41], and the peak at 3,026 cm^{-1} could be attributed to terminal CH_2 absorption [42]. The peak at 2,922 cm^{-1} can be attributed to the stretching vibration of the methylene group with a blueshift [43], indicating that PS interacts with ZIF-8. FT-IR spectral analysis of the PS@ZIF-8 composite particles revealed the presence of distinct characteristic peaks for both components.

The chemical composition and bonding state of the PS@ZIF-8 composite nanomaterials were investigated via X-ray photoelectron spectroscopy (XPS). As shown in Fig. 3(c), the whole XPS spectrum of the composite PS@ZIF-8 containing ZIF-8 contained Zn, C, and N. There were four peaks for PS@ZIF-8 at 284.2, 284.8, 285.6, and 287.8 eV, which correspond to sp2 hybridized carbon (C–C), C=C, C–N, and C=O bonding, respectively (Fig. 3(d)) [44]. The peaks at 1,044.4 and 1,021.4 eV were caused by Zn $2p_{1/2}$ and Zn $2p_{3/2}$, respectively (Fig. 3(f)) [45]. The O 1s peak located at 531.1 eV is a distinct peak attributed to Zn–OH chemical bonding [46]. The N 1s XPS results are shown in Fig. 3(e). In the N 1s spectrum of PS@ZIF-8, a strong peak with a binding energy of 398.7 eV was observed, which was attributed to the C–N bond of ZIF-8 [47, 48]. These results indicate the

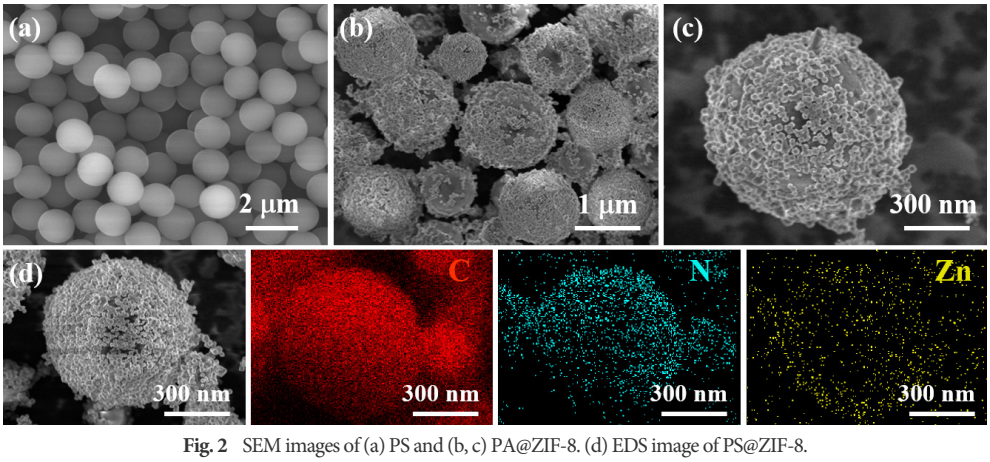

Fig. 2 SEM images of (a) PS and (b, c) PA@ZIF-8. (d) EDS image of PS@ZIF-8.

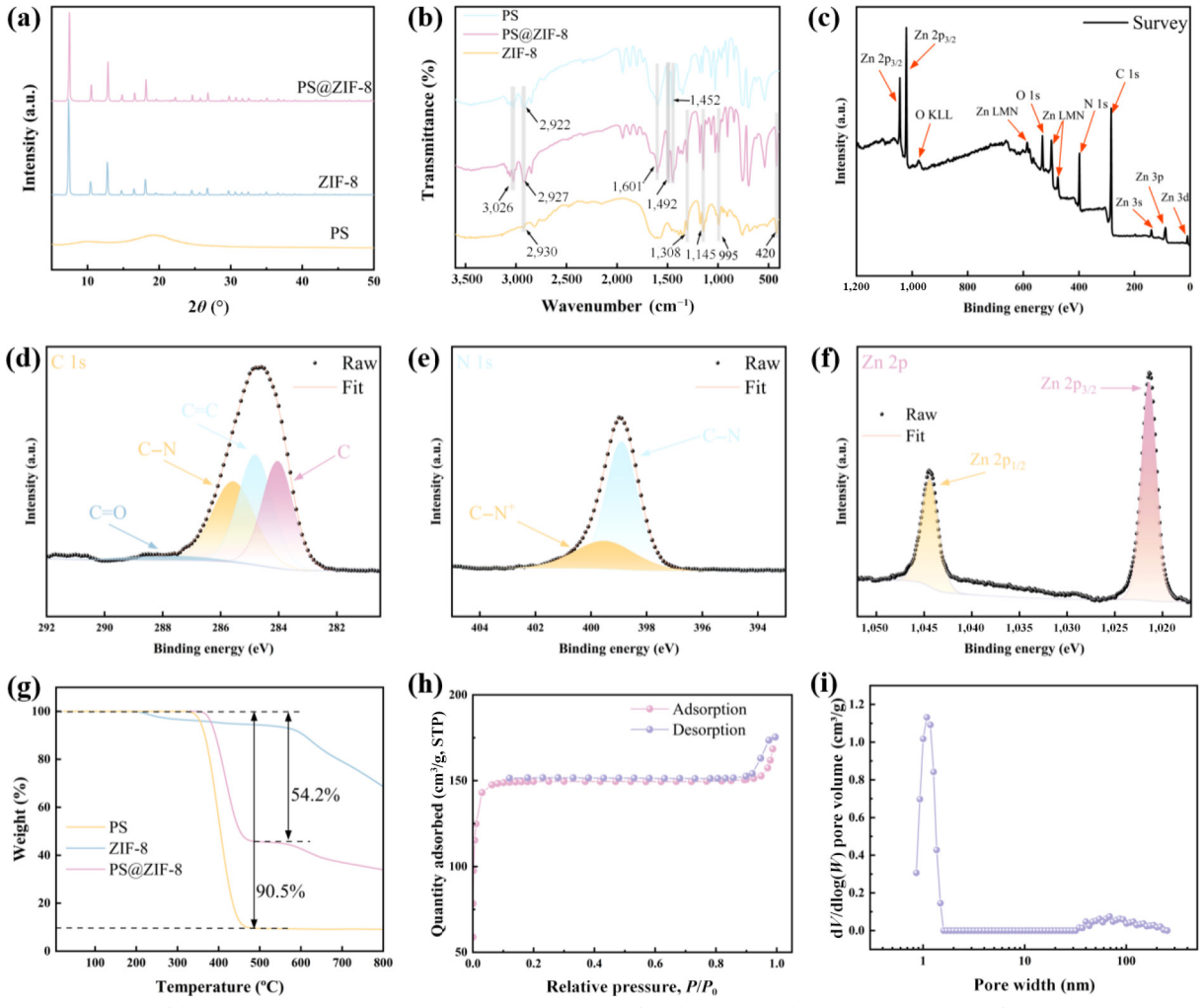

Fig. 3 (a) XRD patterns of the PS particles and PS@ZIF-8 crystals. (b) FT-IR spectra of synthesized PS and PS@ZIF-8. XPS spectra of PS@ZIF-8: (c) survey spectrum and (d–f) high-resolution C 1s, N 1s, and Zn 2p spectra. (g) TGA curves of different samples. (h) N_2 adsorption–desorption isotherms and (i) corresponding pore size distributions of the PS@ZIF-8 particles.

successful preparation of the PS@ZIF-8 composite nanomaterials.

The TGA curves of PS, ZIF-8, and PS@ZIF-8 are shown in Fig. 3(g). The weight loss of PS@ZIF-8 was always lower than that of pure PS from 30 to 800 °C. PS@ZIF-8 exhibited two stages of thermal decomposition in a nitrogen atmosphere. The first decomposition stage occurred in the range of 340–490 °C, which was consistent with the range of PS. Apparently, this was related to the cleavage of PS. The second stage of decomposition occurred between 490 and 800 °C, which exhibited a weight loss step similar to that of ZIF-8. The weight loss can be attributed to the structure of ZIF-8 being broken down. At 800 °C, the residual weight of PS was approximately 9.5%, indicating that most of the composite nanoparticles decomposed into volatile products. In addition, the residual carbon content of PS@ZIF-8 increased to 33.9% at 800 °C. This result could be because PS@ZIF-8 has high thermal stability properties due to the protective effect of ZIF-8. As shown in Fig. 3(h), the prepared PS@ZIF-8 exhibited a typical microporous structure with a Brunauer–Emmett–Teller (BET) surface area of 640 m^2/g. The corresponding distribution curves revealed that ZIF-8 possessed micropores of 8–15 Å (Fig. 3(i)). These results showed that ZIF-8 effectively encapsulated the PS microspheres and provided more active sites, which facilitated frictional contact between the dispersed-phase particles (PS@ZIF-8) and their dispersion in the dispersion medium.

3.2 Rheological properties of the STF samples

For the STF samples, the rheological properties at different concentrations were preferentially studied. As shown in Fig. 4(a), the viscosity of the pure ionic liquid [HOEtMI][NTf_2] initially decreased and then stabilized with increasing shear rate. The stabilized viscosity was approximately 0.08 Pa·s, indicating a shear-thinning phenomenon. As presented in Fig. 4(b), different concentrations of STF samples unavoidably showed shear thickening behavior first in the initial stage. As the shear rate increased, the viscosity of the STF decreased to a certain extent and then started to increase in reverse. When the PS@ZIF-8 concentration increased, the critical shear thickening rate of the STF samples in the shear process decreased, whereas the peak viscosity increased. Surprisingly, the viscosity of the STF containing PS@ZIF-8 at a concentration of 72 wt% in the shear thickening region increased from 3.66 to 284 Pa·s, with a thickening ratio of 77.6. Under the same shear thickening rate, the lowest viscosity of the STF containing PS@ZIF-8 at a concentration of 56 wt% was 0.37 Pa·s, the peak viscosity was 0.66 Pa·s, and the thickening ratio was only 1.7. Increasing the concentration of the dispersed phase (PS@ZIF-8) improved the shear thickening effect of the STF samples. For the same shear scan range, the shear stress vs. shear rate curves exhibited the same trend, with the shear stress increasing with increasing shear rate

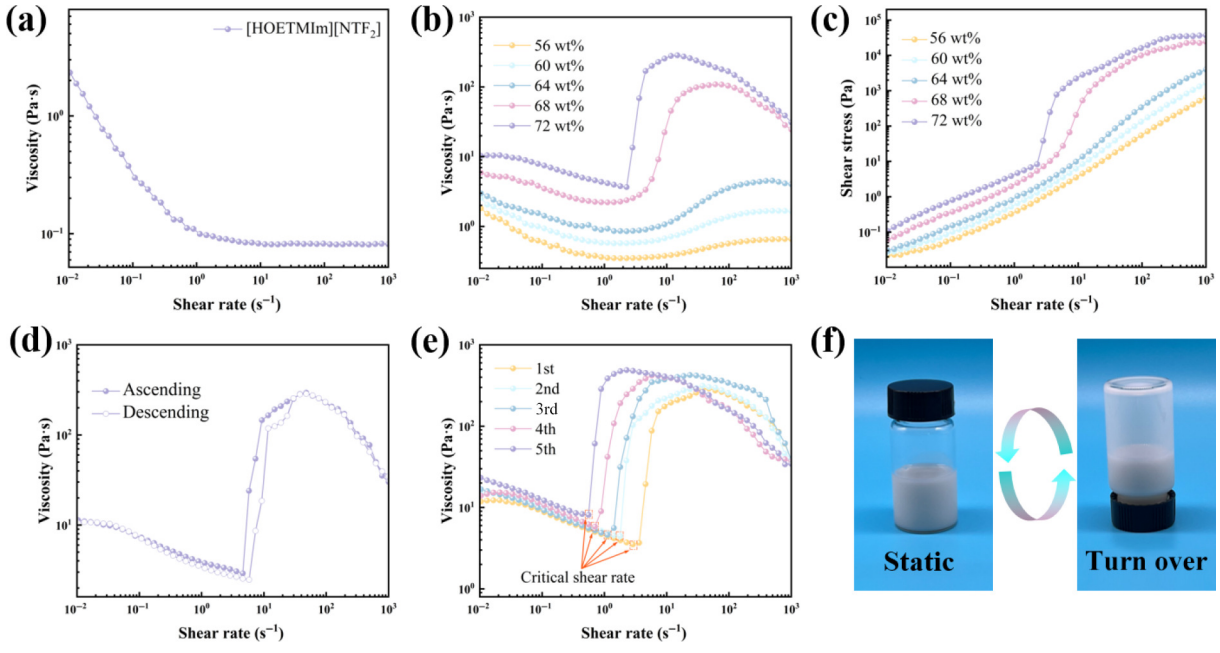

Fig. 4 Relationships between viscosity and shear rate for the (a) IL and (b) STF samples. (c) Relationship between the shear stress and shear rate for the STF samples. (d) Reversible flow curves of 72 wt% STF. (e) Viscosity vs. shear rate curves during multiple shear rate scans for 72 wt% STF. (f) Photographic demonstration of the macroscopic fluidity of the STF samples.

(Fig. 4(c)). The above results indicate that the prepared STF samples have a typical shear thickening effect.

Figure 4(d) shows the reproducibility of the shear thickening behavior of the STF samples containing PS@ZIF-8 particles with a mass fraction of 72 wt% under cyclic loading. The reversible properties of the STF indicate that it is sensitive to the shear rate. This is due to the instability of the nanoparticle clusters formed in the shear thickening region. During the initial phase of the increase in shear rate, the nanoparticle clusters may decrease in size, leading to a gradual decrease in viscosity. Furthermore, the clusters maintained by the lubrication force are dynamic, and as the shear rate decreases and the hydrodynamic force weakens, the clusters disintegrate and are redispersed in the medium. In addition, as the dispersed phase concentration increased, the behavior of the STF samples changed from continuous shear thickening (CST) behavior to discontinuous shear thickening (DST) behavior. Power-law models can be used to characterize the CST-to-DST variation in STFs. By fitting a power-law model to obtain a non-Newtonian exponent n, the system is usually called DST if $n \geqslant 2$ and CST if $1 < n \leqslant 2$. In this case, multiple shear scans were used to investigate the shear thickening stability of the suspension system. Even after the five shear scans shown in Fig. 4(e), the STF containing PS@ZIF-8 (72 wt%) still exhibited obvious shear thickening behavior, whereas the peak viscosity of multiple scans gradually increased, and the critical shear rate gradually decreased. This could be because the shear thickening behavior of the STF samples had good reversibility with a transient response. The good flowability of the 72 wt% STF is shown in Fig. 4(f). Furthermore, the dynamic rheological properties of the STF samples are shown in Figs. 5(a) and 5(b). According to viscoelastic theory, the storage modulus (G') and loss modulus (G'') represent the elastic and viscous strengths of the system, respectively. After reaching the critical strain, both G' and G'' suddenly increase, which indicates a shear thickening effect in the STF system. An increase in G' indicates the aggregation of dispersed-phase particles in the shear thickening region, whereas an increase in G'' indicates energy dissipation in the shear thickening process [49]. When the glass rod was slowly removed from the sample bottle, the STF clearly exhibited shear thinning and appeared to be liquid. However, when the glass rod was quickly lifted from the bottle, the viscosity of the STF increased dramatically, and the container was able to be lifted along with the sample, causing significant shear thickening to occur (Fig. 5(c)).

Through the analysis of all the above data, the mechanism of the shear thickening behavior of the suspension system was determined, and a schematic diagram is shown in Fig. 5(e). The increase in the interaction between the PS@ZIF-8 nanoparticles and the carrier liquid [HOEtMI][NTf_2] was responsible for influencing the shear thickening effect. At equilibrium, the PS@ZIF-8 particles were well dispersed in the dispersion medium. Before the critical shear rate point, the disordered state of the particles under the applied stress led to a change in the formation of a laminar array with increasing shear rate, and the system exhibited shear thinning. After the critical shear rate, when the external force increased to the critical shear stress, the particles in the STF collided with each other during the motion process. Owing to friction and hydrogen bonding forming a contact network, the viscosity of the system significantly increased, resulting in a significant increase in system viscosity. This represented the thickening stage.

It was also found that scaled stress transfer in STF samples was achieved through contact interactions [50]. Since the STF samples are dense suspension–dispersion systems, the particle–medium interactions are disturbed. The increase in the STF sample concentration led to an increase in the interaction force between the particles, thereby reducing the distance between the particles and causing a sharp increase in viscosity. The high-concentration suspension DST was caused by frictional contact, which was consistent with the rheological properties of the STF samples. Additionally, the frictional contact between particles is affected by surface roughness [51]. Zheng et al. [52] reported that stress-activated frictional contact played a key role in the shear thickening phenomenon. Therefore, controlling the surface roughness of the PS nanoparticles had an important effect on improving the DST. The energy storage modulus G' of the 72 wt% STF increased by more than two orders of magnitude when the

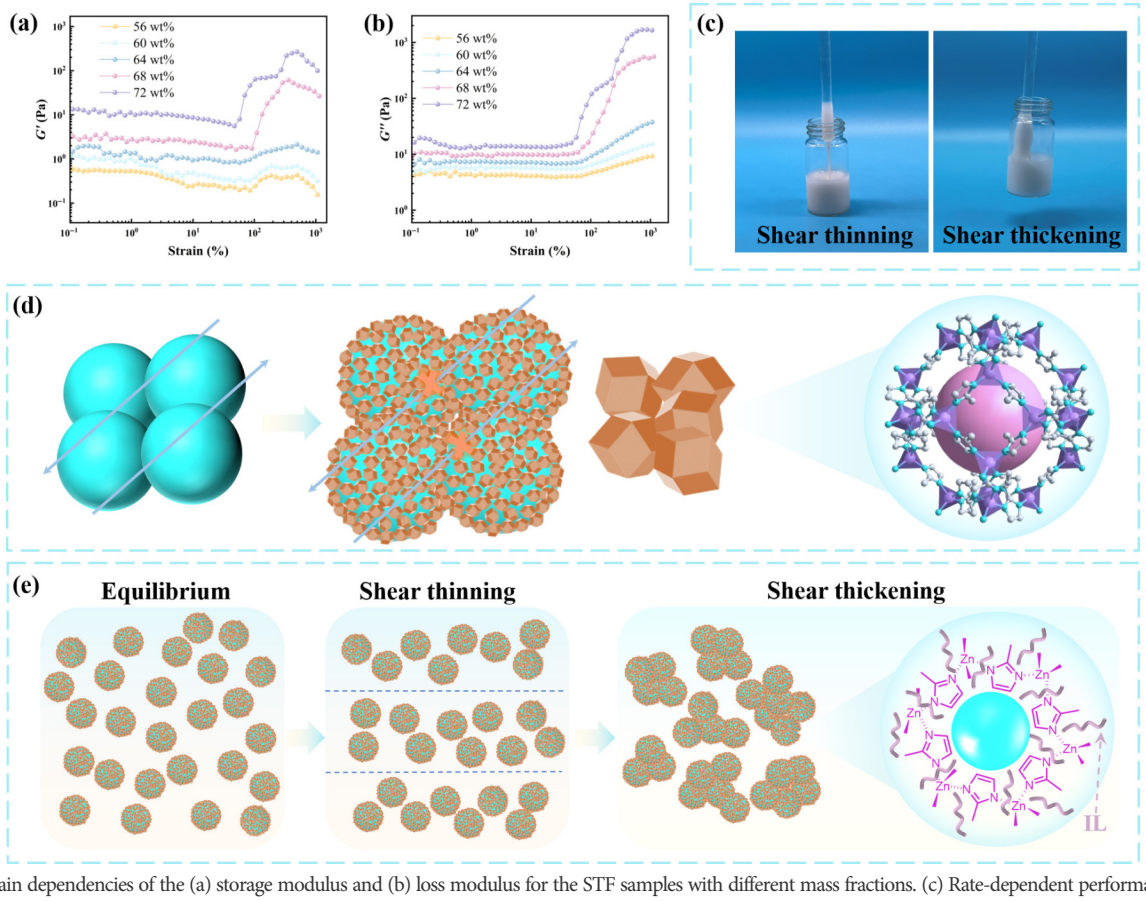

Fig. 5 Strain dependencies of the (a) storage modulus and (b) loss modulus for the STF samples with different mass fractions. (c) Rate-dependent performance of the STF samples. (d) Illustrations of the interactions between the nanoparticles in the STF samples. (e) Microstructural change process of the shear thickening of the STF samples.

strain reached a critical value, which confirmed the strong aggregation in the shear thickening region, and the sharp increase in the energy dissipation modulus G'' also proved that friction was the main force when the concentration of the STF samples reached a certain value. The encapsulation of PS particles by ZIF-8 affected the contact and friction between particle clusters, which in turn had an impact on the influence of the shear thickening process (Fig. 5(d)). The contact at the surface rough spots limited the rolling between the particles. The PS@ZIF-8 particles had difficulty sliding in the STF systems, and frictional contact was prone to occur, which led to a decrease in the critical shear rate. In addition, owing to the high specific area and porous structure of ZIF-8, the ionic liquid [HOEtMI][NTf_2] can diffuse into the micropores of ZIF-8 and can directly interact with ZIF-8 to form a larger frictional contact network, which leads to a sharp increase in the viscosity of the STF samples.

3.3 Dispersion stability of the STF samples

Conventional STF samples face the problem that their shear thickening properties are weakened by the volatilization of the dispersion medium and the settling of dispersed phase particles in dense suspensions. Therefore, the dispersibility and stability of the prepared suspensions were investigated. First, the PS-based STF samples and PS@ZIF-8-based STF samples were transferred into centrifuge tubes for centrifuge stability analysis and evaluation. The centrifugation time was set to 10 min, and the centrifugation speed was set to 8,000 r/min. Upon completion, the solutions were removed from the centrifuge tubes and placed in a graduated cylinder to evaluate the delamination properties of the STF samples. As shown in Fig. 6(a), the STF samples prepared with PS@ZIF-8 as a single dispersed phase exhibited excellent stability without obvious delamination after centrifugation. On the other hand, the delamination property of the STF prepared with pure PS as the dispersed phase was 5.8%, indicating its poor stability. As shown in Fig. 6(b), 64 wt% STF resulted in the best stability under centrifugal conditions, with the lowest delamination property (1.21%) after standing for 10 days. After 30 and 60 days of rest, 60 wt% STF resulted in the lowest delamination properties, whereas 72 wt% STF resulted in the highest delamination properties (Figs. 6(c) and 6(d)). Figure 6(e) shows that the stabilization coefficient tended to first increase but then decrease as the mass fraction of PS@ZIF-8 increased. The stability coefficient of the STF sample with a 64% mass fraction of particles in the dispersed phase remained above 0.98 after standing for 60 days, which was consistent with the centrifugal stability of the STF samples.

Figure 6(f) shows the zeta potential of the STF samples containing different contents of PS@ZIF-8. Similarly, the absolute value first increased but then decreased with increasing dispersed phase content. At contents between 60 and 68 wt%, the zeta potential values did not change significantly (−41.3 to −37.5 mV), but the absolute value decreased significantly when the content of the dispersed phase was greater than 68 wt%. Additionally, 64 wt% STF had a zeta potential of −44.7 mV, which was the highest stability of the suspension system. With increasing PS@ZIF-8 concentration, the particle suspension systems tended to collapse into a dense network, which could be the result of interparticle interactions and the generation of attractive van der Waals forces between solid particles. Moreover, Cao et al. [53] reported that the diffusion layers of different particles in a

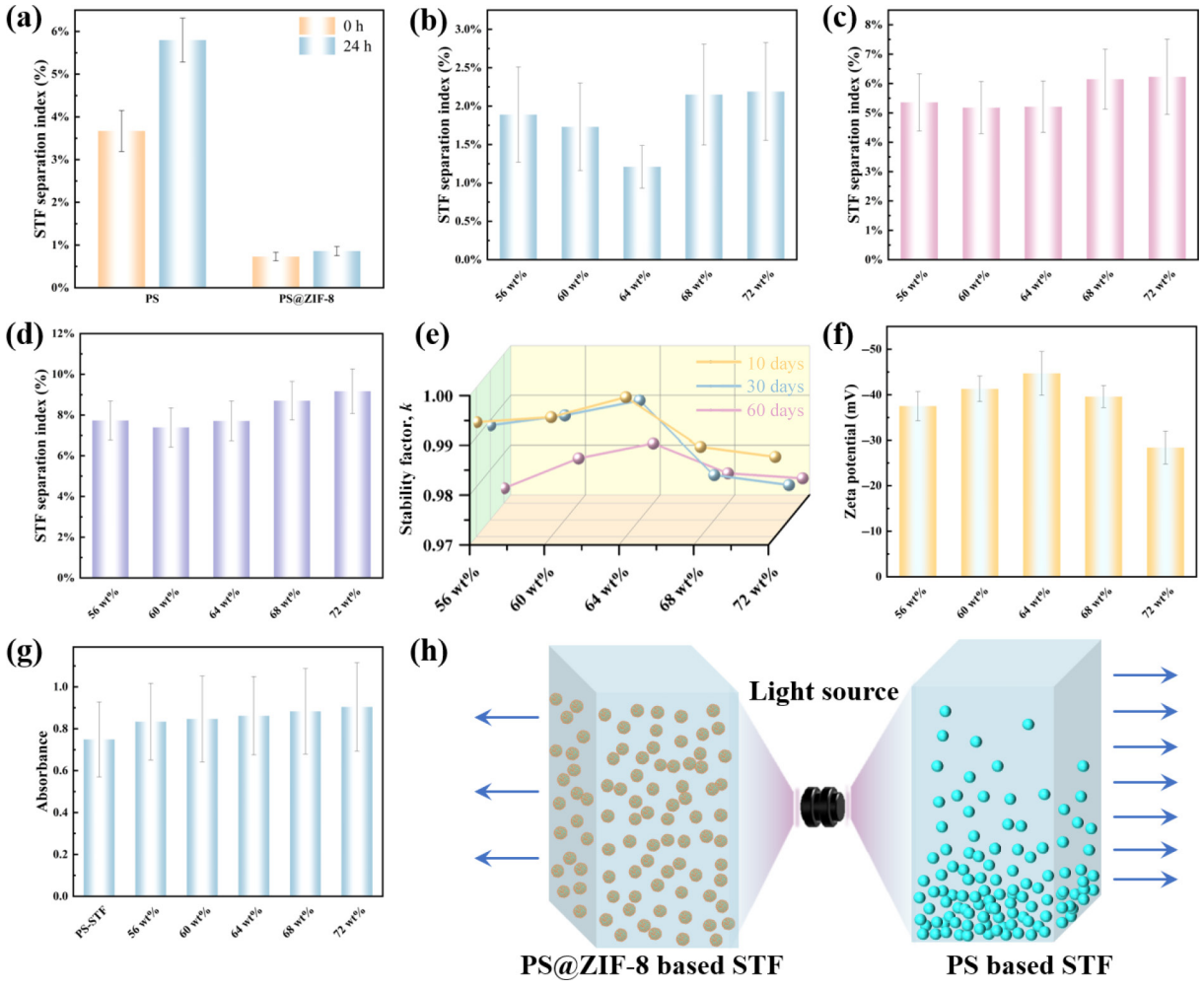

Fig. 6 (a) Centrifugal stability of the STF samples when PS or PS@ZIF-8 was used as the dispersed phase. Centrifugal stability of the PS@ZIF-8-based STF samples after (b) 10 days, (c) 30 days, and (d) 60 days of standing. Centrifugal stability of the PS@ZIF-8-based STF samples after (b) 10 days, (c) 30 days, and (d) 60 days of standing. (e) The sedimentation resistance performance of the PS@ZIF-8-based STF samples. (f) Zeta potential of STF samples with different concentrations. (g) Absorbance of the STF samples after standing for 24 h. (h) Schematic diagram of the effect of the agglomeration of PS and PS@ZIF-8 in the dispersed phase on light transmission.

suspension system can partially overlap. This phenomenon can also occur in the prepared STF samples, which in turn resulted in a decrease in the zeta potential of the STF samples at high solid phase contents.

To further investigate the dispersion stability of the STF samples, a PS-based STF with a content of 72 wt% was prepared to compare and investigate the stability enhancement mechanism. Figure 6(g) shows that the absorbances of all the PS@ZIF-8-based STFs were greater than those of the PS-based STFs, and the dispersibility of the PS@ZIF-8-based STF samples increased with increasing concentration of the dispersing phase. Overall, the absorbance was linearly related to the concentration of dispersed phase particles in the suspension system, and the suspension system with 72 wt% PS@ZIF-8 presented the best dispersion. These results indicate that well-stabilized STF samples were obtained. This could be because imidazolium-based ionic liquids have low volatility and high thermal and chemical stability. Moreover, $[NTf_2]^-$ is a strong hydrogen bond acceptor that can significantly enhance the interfacial interaction with PS@ZIF-8 and form a physical barrier on the surface of the particles to prevent them from agglomerating under static conditions, thereby improving the retention and dispersion stability of the shear thickening system [54]. This also provides a good basis for the shear thickening performance of STF samples. However, the particles of the dispersed phase in the PS-based STF were attracted to each other by the surface effect and aggregated, forming particle aggregates and accelerating the settling rate. As a result, the concentration of particles in the dispersed phase in the supernatant of the system decreased, resulting in a decrease in absorbance and a decrease in dispersibility of the system (Fig. 6(h)).

3.4 Impact wear resistance of the STF samples

The impact wear resistance of the STF samples was investigated via load impact tests in a finite space. As shown in Fig. 7(a), under the same conditions, the peak force captured by the filled STF upon impact of the drop hammer was small. The maximum impact force decreased with increasing mass fraction of PS@ZIF-8. Compared with that of [HOEtMI][NTf2] and 56 wt% STF, the peak force of the 72 wt% STF mixture was attenuated by 48.4% and 39.7%, respectively. Figure 7(b) shows the force sensor signals with time under impact loading for samples with different concentrations of STF. As the concentration of the STF samples increased, their impact force decayed more significantly. This was consistent with the peak viscosity test results of the rheological test of the STF samples. Upon impact, the STF samples achieved impact resistance by attenuating the peak force and extending the buffer time. As shown in Fig. 7(c), the volume of the pure IL was 8.48×10^6 μm^3 with the same number of impact cycles used for the STF samples. Compared with that of [HOEtMI][NTf_2] ionic liquids, the depth of the impact crater corresponding to the STF

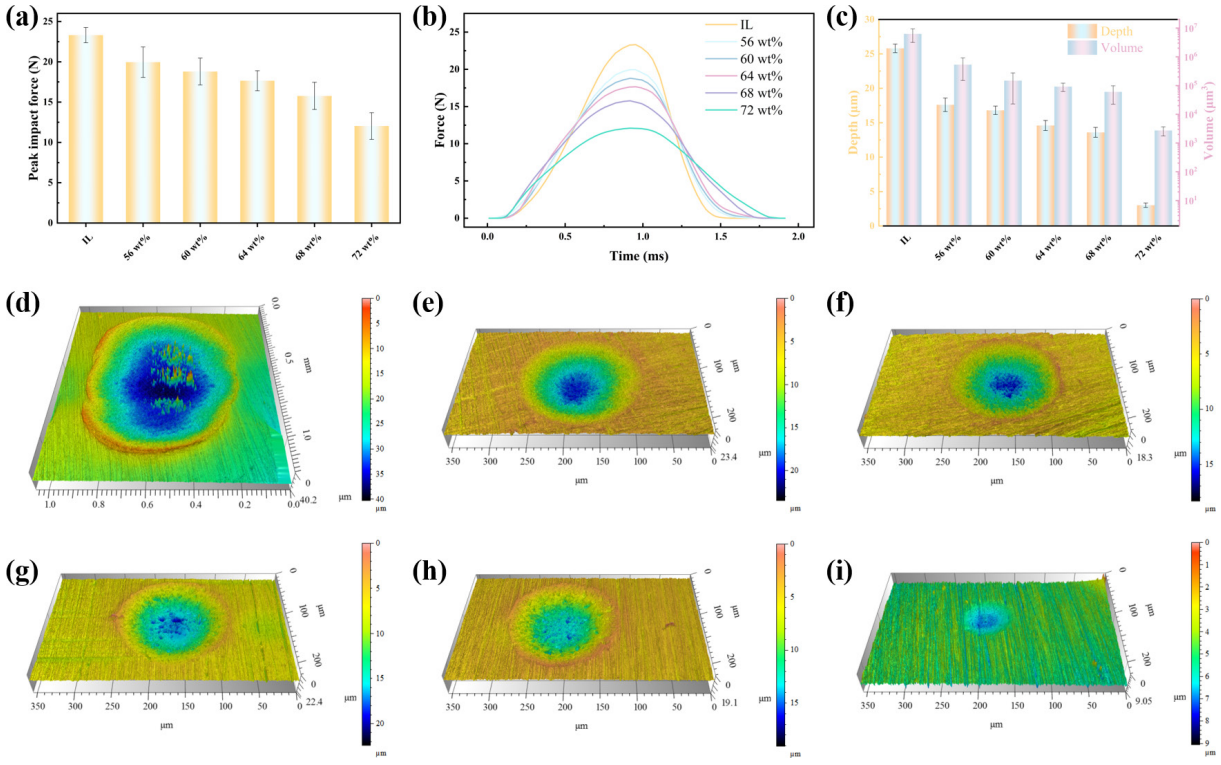

Fig. 7 (a) Peak force for different samples. (b) Force vs. time curves of the IL and STF samples. (c) The depth and volume of the impact craters formed on the surface of the test pieces. 3D morphology of impact craters formed on the test pieces filled with (d) ILs, (e) 56 wt% STF, (f) 60 wt% STF, (g) 64 wt% STF, (h) 68 wt% STF, and (i) 72 wt% STF.

samples was significantly lower, and the volume of the impact crater formed decreased by a relative order of magnitude. In particular, the impact crater volume corresponding to an STF filling of 72 wt% was only 951 μm³. Among these filling materials, 72 wt% STF not only had the smallest peak force but also had the smallest deformation with the corresponding impact crater. The results further indicated that the impact resistance of the filled STF samples corresponded to their rheological properties. Figures 7(d)–7(i) and Fig. S3 in the ESM show the 3D morphology of the impact craters on the sample surface under different conditions. The impact wear produced by the punch on the sample surface significantly improved after the STF samples were filled. The above experiments directly confirmed the anti-impact wear performance of the STF samples. By both filling the STF samples and increasing the concentration of dispersed phase particles, the peak force and deformation of the samples protected by the STF samples can be reduced during the impact process, which indicates that the STF samples could exhibit excellent impact resistance and energy absorption ability, thus achieving better resistance to impact wear.

The reasons for the above phenomenon are as follows. Under impact excitation, force transfer under load impact caused rapid aggregation of dispersed phase particles, which triggered the shear thickening effect. Additionally, the shear thickening effect of the STF samples increased with increasing concentration of the dispersed phase. As the STF viscosity increased and DSTs formed, the STF solidified in a certain area, and the normal resistance to STF formation in the impact direction increased sharply. Increasing the normal resistance to the formation of impacts helped reduce the deformation of the sample and prevented damage to the sample due to the enormous load created by the impact. The large increase in the associated viscosity (DST) in the shock flow field was due to the formation of a network of encircling frictional contacts. Furthermore, these frictional contacts can only be formed when the applied stresses overcome the lubricating forces of the liquid between the particles.

Figure 8 shows a schematic illustration of the evolution of the flow field inside the STF samples under impact loading. For conventional STF samples, ethylene glycol, polyethylene glycol, or other alcohols are used as the dispersion medium. The increase in hydrogen bonding between the dispersed phase particles and the dispersing medium led to the formation of a stronger surface solvent layer on the nanoparticles, i.e., a "lubricated" state between the dispersed phase particles. The introduction of a hydroxyl-functionalized IL as a dispersion medium for the preparation of the STF samples resulted in a relatively weak solvent layer, weakening the steric barrier that prevents frictional contact between the particles. This promotes frictional contact between the particles at low loads. Owing to the different PS@ZIF-8 contents in the STF, two states of internal particle arrangement may exist when shear thickening occurs in the prepared STF system. When the ZIF-8 content is relatively low, impact excitation causes the particles to begin to aggregate and form particle clusters. For suspension systems with higher solids contents, PS@ZIF-8 particles in the impact field form particle aggregates throughout the impact flow field. The particle clusters in the suspension flow field that are in contact with different impacts have different rates of movement, and the clusters become clogged in the impact flow field. With the introduction of ZIF-8 in the STF, the interparticle interactions in the STF increased the face–face contact between the particles in addition to the point–point contact of the spherical PS. In the low-pressure region, neighboring particles are separated by a gap filled with carrier fluid. In the high-pressure region at the shock front, the impact triggers the shear thickening behavior of the STF, the destruction of the interparticle "lubrication" in the suspension, and the formation of hard frictional contacts, which results in the expulsion of a portion of the dispersed medium between the

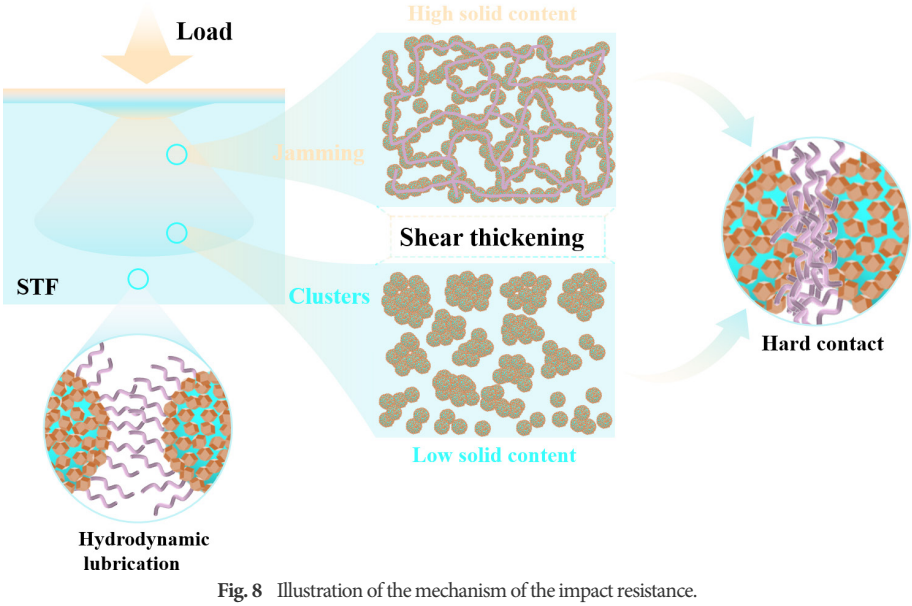

Fig. 8 Illustration of the mechanism of the impact resistance.

nanoparticles. As a result, the high proportion of solids inside the STF creates strong internal friction when subjected to impact, which also leads to an increase in energy dissipation. In summary, the STF exhibited shear thickening behavior during a short period of load impact, resulting in excellent impact wear resistance.

4 Conclusions

In summary, PS@ZIF-8 composites with a core–shell structure were successfully synthesized as the dispersed phase and dispersed in ionic liquids to obtain a novel STF. Owing to the perfect cooperation between the PS@ZIF-8 particles and the ionic liquid, this STF demonstrated excellent shear thickening performance in steady-state and dynamic rheological tests. By adjusting the content of dispersed phase particles, the rheological behavior of the STF samples can be regulated from continuous shear thickening to discontinuous shear thickening (with a thickening ratio of up to 77.6). The excellent thickening performance of the STF can be attributed to the unique porous core–shell structure of PS@ZIF-8, as well as the formation of a stable frictional contact network between the dispersed phase and the dispersion medium. In addition, the development of an STF requires controlling the settling of the dispersed phase to improve the ability of the particle suspension, which is required as a protective structure to improve the dispersibility and stability of the STF. This study revealed that PS@ZIF-8-based STF samples can help address these shortcomings and expand their potential applications. Moreover, the PS@ZIF-8 ionic liquid composite systems achieved good impact resistance and wear protection for the filled structures. Compared with that of the pure PS-based STF, the energy dissipation performance of the PS@ZIF-8-based STF as a protective structure was significantly improved. At a PS@ZIF-8 content of 72 wt%, the prepared STF showed excellent energy dissipation under impact loading. This work not only provides a new type of STF for shear thickening systems but also opens a new opportunity to fabricate advanced dispersion systems to improve the dispersion stability and impact wear resistance of suspension systems.

Acknowledgements

This work was financially supported by the Strategic Priority Research Program of the Chinese Academy of Sciences (No. XDB0470301), the Key Research and Development Program of Shandong Province (No. 2022CXGC020309), and the Gansu Provincial Science and Technology Plan Project (Nos. 23ZDKA012 and 23ZDKA0003).

Declaration of competing interest

The authors have no competing interests to declare that are relevant to the content of this article.

Electronic Supplementary Material

Supplementary material is available in the online version of this article at https://doi.org/10.26599/FRICT.2025.9441068.

References

[1] Poletto J C, Neis P D, Fauconnier D, Ramalho A, De Baets P, Ferreira N F. A systematic investigation of grooving and rolling abrasive mechanisms using surface topography. *Wear* **548**: 205389 (2024)

[2] Xu N, Wang C, Yang L Q, Jose G, Morina A. Probing the tribochemical impact on wear rate dynamics of hydrogenated amorphous carbon via Raman-based profilometry. *ACS Appl Mater Inter* **14**(1): 2071–2081 (2022)

[3] Zhang J S, Wang Y, Zhou J Y, Wu J P, Liu S, Sang M, Liu B, Pan Y C, Gong X L. Multi-functional STF-based yarn for human protection and wearable systems. *Chem Eng J* **453**: 139869 (2023)

[4] Fernandez N, Mani R, Rinaldi D, Kadau D, Mosquet M, Lombois-Burger H, Cayer-Barrioz J, Herrmann H J, Spencer N D, Isa L. Microscopic mechanism for shear thickening of non-Brownian suspensions. *Phys Rev Lett* **111**(10): 108301 (2013)

[5] Tan D Q, Yang X Q, He Q, Gao H Y. Failure behavior of cemented carbide under impact-sliding wear conditions. *Mater Trans* **62**(9): 1336–1342 (2021)

[6] Chen P, Chen S D, Huang Q Y, Zhang W, Li Z L, Wu H, Shan Q. Study on the correlation mechanism between wear failure behavior and the TRIP effect of retained austenite in bainitic steel. *Tribol Lett* **71**(3): 79 (2023)

[7] Chen J L, He K F, Fei J J, Yu J Y, Meng Z Y, Pang Y Y, Liang L Z, Tian Z Q. Extreme pressure and anti-wear properties of polycarboxylate superplasticizer modified 3D porous graphene/SiO_2 as water-based lubricant additives. *Wear* **540–541**: 205239 (2024)

[8] Wang Z J, Zhou M J, Jiang Y H, Sui Y D, Li Z L. Impact-abrasive wear property of ZrO_2 toughened Al_2O_3 ceramic particles reinforced high manganese steel matrix composites. *Tribol Int* **194**: 109547 (2024)

[9] Pan Y C, Sang M, Zhang J S, Sun Y X, Liu S, Hu Y, Gong X L. Flexible and lightweight Kevlar composites towards flame retardant and impact resistance with excellent thermal stability. *Chem Eng J* **452**: 139565 (2023)
[10] Shah P, Arora S, Driscoll M M. Coexistence of solid and liquid phases in shear jammed colloidal drops. *Commun Phys* **5**: 222 (2022)
[11] Comtet J, Chatté G, Niguès A, Bocquet L, Siria A, Colin A. Pairwise frictional profile between particles determines discontinuous shear thickening transition in non-colloidal suspensions. *Nat Commun* **8**: 15633 (2017)
[12] Brown E, Jaeger H M. Shear thickening in concentrated suspensions: Phenomenology, mechanisms and relations to jamming. *Rep Prog Phys* **77**(4): 046602 (2014)
[13] Hao J L, Ding J, Rutledge G C. Shape-stable composites of electrospun nonwoven mats and shear-thickening fluids. *ACS Appl Mater Inter* **14**(6): 8373–8383 (2022)
[14] Liu Q, Liu B, Pan Y C, Zhang J S, Wang K, Lou C C, Zhou J Y, Deng H X, Gong X L. Probing the roles of surface characteristic of suspended nanoparticle in shear thickening suspensions. *Appl Surf Sci* **659**: 159910 (2024)
[15] Hai T, Mohammed Alhomayani F, Sharma K. Dynamic impact and tensile strength characteristics of novel shear thickening fluid (STF)-treated fabric and modeling tensile strength using artificial intelligence. *J Mol Liq* **387**: 122592 (2023)
[16] Gürgen S, Sofuoğlu M A. Vibration attenuation of sandwich structures filled with shear thickening fluids. *Compos Part B Eng* **186**: 107831 (2020)
[17] Montenegro M, Campo-Deaño L, Galindo-Rosales F J. Formulating, assessing and using shear thickening fluids for cork helmet liners. *Compos Struct* **327**: 117707 (2024)
[18] Bosco A, Paiva F, Odenbach S, Calado V. Influence of particle shape and sample preparation on shear thickening behavior of precipitated calcium carbonate suspensions. *Adv Powder Technol* **32**(3): 802–809 (2021)
[19] Li D Y, Liu T, Zhang J, Qian N B, Lu Z Q, Chang C T, Wang R, Xiao Q, Qi J, You F F. Enhanced dynamic stab resistance and UV-resistance of flexible and lightweight Kevlar fabrics impregnated with multi-phase shear thickening fluid. *J Mater Res Technol* **29**: 2533–2543 (2024)
[20] Das P K, Dash S K, Ganguly R, Santra A K, Venkatesan E P, Rajhi A A, Shaik S, Afzal A. Effect of particle loading and temperature on the rheological behavior of Al_2O_3 and TiO_2 nanofluids. *Energy Sources Part A Recovery Util Environ Eff* **44**(3): 7062–7079 (2022)
[21] Wu Y X, Wang W H, Zhang J S, Sang M, Xu Y Q, Zhou J Y, Wang S, Cai Y B, Xuan S H, Gong X L. Liquid or solid? A biologically inspired concentrated suspension for protective coating. *Chem Eng J* **428**: 131793 (2022)
[22] Sheikhi M R, Hasanzadeh M, Gürgen S, Li J. Enhanced anti-impact resistance of polyurethane foam composites with multi-phase shear thickening fluids containing various carbon nanofillers. *Mater Today Commun* **38**: 107991 (2024)
[23] Chen S S, Zhao Y, Zhang H, Xu P D, Jiang Z Y, Zhang H, Yang J L. Direct microencapsulation of Ionic-Liquid-Based shear thickening fluid via rheological behavior transition for functional applications. *Chem Eng J* **455**: 140819 (2023)
[24] Liu W P, Zheng B Q, Yin X C, Yu X X, Zhang Y G, Wiegart L, Fluerasu A, Armstrong B L, Veith G M, Bhatia S R. XPCS microrheology and rheology of sterically stabilized nanoparticle dispersions in aprotic solvents. *ACS Appl Mater Inter* **13**(12): 14267–14274 (2021)
[25] Zhang X, Wang P F, Kurkin A, Chen Q, Gong X L, Zhang Z, Yang E H, Yang J L. Mechanical response of shear thickening fluid filled composite subjected to different strain rates. *Int J Mech Sci* **196**: 106304 (2021)
[26] Sheng X Z, Qin J B, Wang T W, Yun J, Zhang G C. Properties of Kevlar fabric composites reinforced by STF composed of monodisperse polystyrene microspheres. *Thin Wall Struct* **167**: 108238 (2021)
[27] Cao S S, Pang H M, Zhao C Y, Xuan S H, Gong X L. The CNT/PSt-EA/Kevlar composite with excellent ballistic performance. *Compos Part B Eng* **185**: 107793 (2020)
[28] Taheri M, Ashok D, Sen T, Enge T G, Verma N K, Tricoli A, Lowe A, Nisbet D R, Tsuzuki T. Stability of ZIF-8 nanopowders in bacterial culture media and its implication for antibacterial properties. *Chem Eng J* **413**: 127511 (2021)
[29] Li Y X, Yan L H, Liu G H, Chen H X, Zhao H, Wang L H, Gao J, Liu Y T, Zheng X B, Jiang Y J. Enhanced electroenzymatic CO_2 reduction by a multifunctional ZIF-8 layer on silica nanoflower with immobilized enzyme. *Chem Eng J* **466**: 143198 (2023)
[30] Luo D C, Chang C R, Hu Z. One-step encapsulation of TBAB in ZIF-8 for CO_2 fixation: Revealing the synergistic mechanism between TBAB and ZIF-8. *ACS Catal* **14**(14): 11101–11112 (2024)
[31] Wang F F, Liu Z, Cheng Z L. High performance of MOF-structured lubricating material with nano- and micro-sized morphologies. *Mater Lett* **248**: 222–226 (2019)
[32] Niu W X, Yuan M, Wang P F, Shi Q, Xu H, Dong J X. One-pot synthesis of SIB@ZIF-8 with enhanced anti-corrosion properties and excellent lubrication properties. *Tribol Int* **151**: 106491 (2020)
[33] Liu L, Zhang Y, Qiao Y J, Tan S C, Feng S F, Ma J, Liu Y H, Luo J B. 2D metal-organic frameworks with square grid structure: A promising new-generation superlubricating material. *Nano Today* **40**: 101262 (2021)
[34] Liu J X, Qian Y, Li D S, Wu W, Zhang M C, Yan J, Li B, Zhou F. Oil-soluble polymer brushes-functionalized nanoMOFs for highly efficient friction and wear reduction. *Friction* **12**(7): 1499–1511 (2024)
[35] Jia Q, Lai B B, Dou X H, Han Y Q. Intelligent response protection of a multi-phase shear thickening fluid based on ZIF-8 modulated rheological properties for impact loading. *Tribol Int* **192**: 109267 (2024)
[36] Qin J B, Guo B R, Zhang L, Wang T W, Zhang G C, Shi X T. Soft armor materials constructed with Kevlar fabric and a novel shear thickening fluid. *Compos Part B Eng* **183**: 107686 (2020)
[37] Pan Y C, Sang M, Zhang J S, Li Z M, Liu S, Zhang Z T, Ma Q, Gong X L. An integrative warning-protection shear thickened composite sponge towards sensing performance and impact resistance with excellent flame retardant. *Compos Part B Eng* **279**: 111466 (2024)
[38] Xu F, Tian B Y, Cui K, Liu M Y, Yao Y Y, Li H L, Dong R, Fan M J, Cai M R, Zhou F, et al. Fortified lubricating response to sustainable PEG system from protic ionic liquid and their strong hydrogen bonding network. *ACS Sustain Chem Eng* **12**(13): 5343–5355 (2024)
[39] Dong M Y, Zhang K Y, Wan X Y, Wang S L, Fan S K, Ye Z Z, Wang Y Q, Yan Y G, Peng X S. Stable two-dimensional nanoconfined ionic liquids with highly efficient ionic conductivity. *Small* **18**(14): 2108026 (2022)
[40] Yang Q H, Yang C C, Lin C H, Jiang H-L. Metal–organic-framework-derived hollow N-doped porous carbon with ultrahigh concentrations of single Zn atoms for efficient carbon dioxide conversion. *Angew Chem Int Edit* **58**(11): 3511–3515 (2019)
[41] Son H S, Kim K H, Kim J H, Yoon K H, Lee Y S, Paik H J. High-performance shear thickening of polystyrene particles with poly (HEMA). *Colloid Polym Sci* **296**(9): 1591–1598 (2018)
[42] Song K, Wan H. Preparation of carboxyl modification polystyrene microspheres and rheological properties of its polyethylene glycol suspensions. *Polymer Materials Science & Engineering* **34**(5): 170–176 (2018) (in Chinese)
[43] Song K J, Wan H J, Huang H J, Wang X M. Study on rheological property for polystyrene & acrylic acid composite particle/ethylene glycol system. *New Chemical Materials* **45**(11): 143–146 (2017) (in Chinese)
[44] Chen W Q, Li L Y, Li L, Qiu W H, Tang L, Xu L, Xu K J, Wu M H. MoS_2/ZIF-8 hybrid materials for environmental catalysis: Solar-driven antibiotic-degradation engineering. *Engineering* **5**(4): 755–767 (2019)
[45] Zhang Y N, Pei Z, Wang Z H, Wang C E, Liang F F, Wei L Q. ZIF-8

modified by isocyanate as a photocatalytic antibacterial agent. *Rare Metals* **43**(6): 2708–2718 (2024)
[46] Yao Y, Liao G L, Cui H N, Dong W B, Zhao Z. Monodispersed In_2O_3@ZIF-8 core–shell nanocomposite with selectivity and enhanced photocatalytic activity. *J Mater Sci Mater El* **34**(18): 1445 (2023)
[47] Zhang Y J, Li Q Z, Liu C X, Shan X G, Chen X, Dai W X, Fu X Z. The promoted effect of a metal-organic frameworks (ZIF-8) on Au/TiO_2 for CO oxidation at room temperature both in dark and under visible light irradiation. *Appl Catal B Environ* **224**: 283–294 (2018)
[48] Yao Y, Li Z F, Song Y Q, Zhang Y M, Xie K M. Atomically dispersed Ag implanted zeolitic imidazolate frameworks-8 for visible-light enhanced plasmonic opto-chemical sensor. *Chem Eng J* **487**: 150769 (2024)
[49] Wang Q S, Sun R J, Yao M, Chen M Y, Feng Y. The influence of temperature on inter-yarns fictional properties of shear thickening fluids treated Kevlar fabrics. *Compos Part A Appl S* **116**: 46–53 (2019)
[50] Royer J R, Blair D L, Hudson S D. Rheological signature of frictional interactions in shear thickening suspensions. *Phys Rev Lett* **116**(18): 188301 (2016)
[51] Hsu C P, Ramakrishna S N, Zanini M, Spencer N D, Isa L. Roughness-dependent tribology effects on discontinuous shear thickening. *Proc Natl Acad Sci USA* **115**(20): 5117–5122 (2018)
[52] Zheng J Z, Liu Q, Wei W, Lu Y, Wang S X, Chen H X, Zhou Y. Roughness surface of raspberry-shaped silica nanoparticles effect on shear thickening colloidal suspensions. *Appl Surf Sci* **606**: 154917 (2022)
[53] Cao C Z, Luo Y, Xiao M. Preparation and characterization of imidazolyl ionic liquid-based shear thickening dispersion system. *J Appl Polym Sci* **138**(4): 49719 (2021)
[54] Chen B, Wu K, Yang Y, Wang N, Liu Y, Hu S, Wang J, Wen J, Hu S, Chen Q, Shen X, Peng S. A uranium capture strategy based on self-assembly in a hydroxyl-functionalized ionic liquid extraction system. *Chem Commun* **55**(48): 6894–6897 (2019)

Bingbing Lai received her Ph.D. degree in 2019 at Huazhong University of Science and Technology, China. She is an associate professor at the State Key Lab of Solid Lubrication at the Lanzhou Institute of Chemical Physics, Chinese Academy of Sciences, China. She has authored or co-authored more than 20 journal papers. Her research focuses on the synthesis of intelligent lubricating materials, task-specific lubricant additives, and environmentally friendly lubricants.

Qin Zhao received his Ph.D. degree in 2014 at Lanzhou Institute of Chemical Physics, Chinese Academy of Sciences, China. He is an associate professor at the State Key Lab of Solid Lubrication at the Lanzhou Institute of Chemical Physics, Chinese Academy of Sciences, China. He has authored or co-authored more than 30 journal papers. His research interests include ionic liquid lubricants and additives, nanocomposite additives, and lubricating grease materials.

Gaiqing Zhao received her Ph.D. degree in 2012 at Lanzhou Institute of Chemical Physics, Chinese Academy of Sciences, China. She is a full professor at the State Key Lab of Solid Lubrication at Lanzhou Institute of Chemical Physics, Chinese Academy of Sciences, China. She has authored or co-authored more than 50 journal papers. Her research interests are tribochemistry, lithium-based grease, lithium-based complex grease, and high-performance applications.